Near-Field Prediction in Complex Environment Based on Phaseless Scanned Fields and Machine Learning

Jun Wen, *Student Member, IEEE*, Xing-Chang Wei , *Senior Member, IEEE*, Yong-Liang Zhang ,
and Tian-Hao Song

Abstract—The field prediction of an unknown electromagnetic interference (EMI) source within a complex electromagnetic environment requires complex radiation field formulas. In this article, we propose an artificial neural network (ANN) method to predict the field by using the scanned phaseless near-field from the EMI source. The near-field magnitude is scanned using a near-field probe first. After that, an ANN is trained to present the mapping between the observation point and the radiation field. A set of free-space Green's functions are used as the input of the ANN, and the magnitude of the radiation field is taken as the output of the ANN. With the help of Green's function, the trained ANN can accurately predict the radiation field outside the scanning regions. The feasibility of this method is verified using numerical and measurement experiments. The proposed method can realize source reconstruction in a complex electromagnetic environment.

Index Terms—Artificial neural network (ANN), electromagnetic interference (EMI), field prediction, interpolation method.

I. INTRODUCTION

WITH the miniaturization and complication of modern electronic devices, increased working frequency makes electromagnetic interference (EMI) problems more serious [1]. When the internal structure and materials of the devices under test (DUT) are known, full-wave simulation software can be used to simulate and analyze such EMI problems. However, for DUTs in a complex working environment, it is extremely difficult and time consuming to use the full-wave simulation software to model and analyze EMI problems.

The near-field scanning method can capture the radiation features of a real EMI source, which can be helpful to reconstruct an equivalent source to predict the radiation from the real source. According to the principle of equivalence, equivalent magnetic/electric currents can replace the radiating source, where the near-field to near/far-field transformation is accomplished [2]. For the practical EMI source reconstruction, an electric/magnetic dipole array, instead of continuous magnetic/electric currents, is used as the equivalent source. Once the equivalent dipole array is determined, the near-field in other regions can be calculated.

Many methods for reconstructing the equivalent dipole array have been proposed, such as the iteration method [3], the genetic algorithm [4], the differential evolution (DE) method [5], and the dipole extraction from magnitude-only electromagnetic-field data based on genetic algorithm and back-and-forth iteration algorithm [6]. However, not all radiation sources can be accurately reconstructed using the aforementioned methods. Most of the available methods assume that the equivalent dipole array is in the free space or above an infinite ground plane. It is not true for a complex EMI environment, where multireflections and diffractions may exist. Therefore, it is crucial to find a new mapping function between the near-field and the equivalent source.

As a new method, artificial neural network (ANN) shows its potential benefit in the electromagnetic modeling and design, including the inverse modeling and application to microwave filters [7], predicting eye diagram [8], combining with the finite difference time-domain method [9] or the method of moments [10]. It is also used to reconstruct the equivalent dipole of a real EMI source in [11] and [12]. Recently, the powerful self-learning and nonlinear mapping capabilities of ANN are used for radiation source reconstruction in complex environments [13]. However, it requires an accurately measured phase of the near-field and the problem under study is linear. The accurate near-field phase may not be available due to environmental noise.

In this article, the ANN for solving such a problem is proposed. Compared with [13], the process of measuring the phase is eliminated, and the solution of linear equations is transformed into the solution of nonlinear equations. For this purpose, Bayesian regularization is added to improve the nonlinear ability. At the same time, the ANN algorithm is rearranged and presented as "finding the expression of the unknown function f" in Section IIA of this article, instead of the "matrix-vector multiplication" in Section II of the article [13].

The rest of this article is organized as follows. In Section II, we propose an ANN structure based on magnitude-only near-field
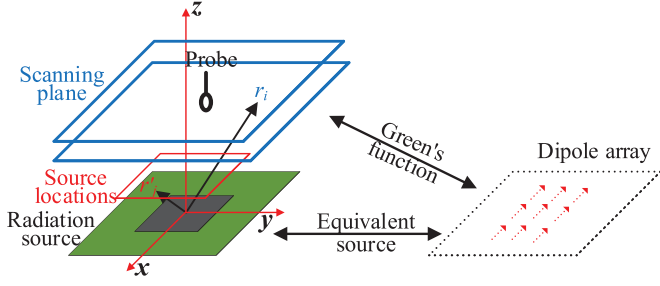
Fig. 1.   EMI source in a complex environment and its equivalent dipole array.

radiation. In Section III, we describe the effectiveness of the proposed method with several numerical examples. Furthermore, the proposed method is demonstrated by using a fabricated antenna placed between two parallel metal plates in Section IV. Finally, Section V gives the conclusion of this article.

II. PROPOSED ANN STRUCTURE

A. Green's Functions Used as ANN Inputs

According to the field equivalence principle, an equivalent dipole array can replace the real and complex EMI radiation source (the DUT), as shown in Fig. 1. In this way, the complex radiation problem can be simplified. In printed circuit board applications, the magnetic field can be more accurately measured than the electric field. Therefore, the scanned magnetic near-field magnitude is usually used to reconstruct the equivalent magnetic dipole array. In Fig. 1, the magnetic near-field distribution of the DUT is scanned by using a magnetic probe, and it is further used to solve the equivalent dipole array inversely. The position and the number of dipoles are all predetermined according to DUT and the scanned field pattern. The unknowns are the moments of every dipole in the array.

In a spherical coordinate system, the free-space Green's function is used to describe the relationship between a z-polarized magnetic dipole located at the origin and its magnetic near-field as

$$
\begin{cases}
H_R = \frac{k_0^2 M}{2\pi\eta}\cos\theta\left(\frac{1}{(k_0 R)^2} - \frac{j}{(k_0 R)^3}\right)e^{-jk_0 R} \\
H_\theta = \frac{jk_0^2 M}{4\pi\eta}\sin\theta\left(\frac{1}{k_0 R} - \frac{j}{(k_0 R)^2} - \frac{1}{(k_0 R)^3}\right)e^{-jk_0 R} \\
H_\varphi = 0
\end{cases} \quad (1)
$$

where M is the dipole moment. The distance between the dipole and the observation point is R, and η and k_0 are the free-space impedance and wavenumber, respectively.

The tangential magnetic near-field on a scanning plane can be expressed as the field summation from all equivalent dipoles (including their images if there is a ground plane) as

$$
\boldsymbol{H}\left(\boldsymbol{r}_i\right) = \sum_{j=1}^{N}\overline{\boldsymbol{G}}\left(\boldsymbol{r}_i, \boldsymbol{r}_j'\right) \cdot \boldsymbol{M}\left(\boldsymbol{r}_j'\right) \quad (2)
$$

where $\boldsymbol{H}(\boldsymbol{r}_i) = [H_x(\boldsymbol{r}_i), H_y(\boldsymbol{r}_i)]^t$ is the scanned tangential magnetic field at the scanning/observation point $\boldsymbol{r}_i$ on the scanning plane. $i = 1,\ldots,M$ and M is the number of scanning points. $\boldsymbol{M}(\boldsymbol{r}_j') = [M_x(\boldsymbol{r}_j'), M_y(\boldsymbol{r}_j')]^t$ is the moment of dipole located

at $\boldsymbol{r}_j'$, and $\overline{\boldsymbol{G}}(\boldsymbol{r}_i, \boldsymbol{r}_j') = \begin{bmatrix} G_{xx}(\boldsymbol{r}_i, \boldsymbol{r}_j'), G_{xy}(\boldsymbol{r}_i, \boldsymbol{r}_j') \\ G_{yx}(\boldsymbol{r}_i, \boldsymbol{r}_j'), G_{yy}(\boldsymbol{r}_i, \boldsymbol{r}_j') \end{bmatrix}$ includes Green's functions obtained from (1). $\boldsymbol{r}_j'$ ($j = 1,\ldots,N$ and N is the number of equivalent dipoles) is named as the source location, which is predetermined according to DUT and the scanned field pattern.

Traditionally, (2) is reduced to a set of linear equations, and then $\boldsymbol{M}(\boldsymbol{r}_j')$ is obtained from the scanned $\boldsymbol{H}(\boldsymbol{r}_i)$. Now let us consider (2) in another way, i.e., $\boldsymbol{H}(\boldsymbol{r}_i)$ is taken as an unknown function of $\overline{\boldsymbol{G}}(\boldsymbol{r}_i, \boldsymbol{r}_j')$ as

$$
\boldsymbol{H}\left(\boldsymbol{r}_i\right) = \boldsymbol{f}\begin{bmatrix} G_{xx}\left(\boldsymbol{r}_i, \boldsymbol{r}_1'\right), G_{xx}\left(\boldsymbol{r}_i, \boldsymbol{r}_2'\right), \ldots, G_{xx}\left(\boldsymbol{r}_i, \boldsymbol{r}_N'\right), \\ G_{xy}\left(\boldsymbol{r}_i, \boldsymbol{r}_1'\right), G_{xy}\left(\boldsymbol{r}_i, \boldsymbol{r}_2'\right), \ldots, G_{xy}\left(\boldsymbol{r}_i, \boldsymbol{r}_N'\right), \\ G_{yx}\left(\boldsymbol{r}_i, \boldsymbol{r}_1'\right), G_{yx}\left(\boldsymbol{r}_i, \boldsymbol{r}_2'\right), \ldots, G_{yx}\left(\boldsymbol{r}_i, \boldsymbol{r}_N'\right), \\ G_{yy}\left(\boldsymbol{r}_i, \boldsymbol{r}_1'\right), G_{yy}\left(\boldsymbol{r}_i, \boldsymbol{r}_2'\right), \ldots, G_{yy}\left(\boldsymbol{r}_i, \boldsymbol{r}_N'\right) \end{bmatrix}.
$$
$$(3)$$

The total number of Green's functions in (3) is $4N$. As long as the source locations $\boldsymbol{r}_j'$ ($j = 1,\ldots,N$) are given, the values of $G_{xx}(\boldsymbol{r}_i, \boldsymbol{r}_j')$, $G_{xy}(\boldsymbol{r}_i, \boldsymbol{r}_j')$, $G_{yx}(\boldsymbol{r}_i, \boldsymbol{r}_j')$, and $G_{yy}(\boldsymbol{r}_i, \boldsymbol{r}_j')$ in (3) only change with the observation point $\boldsymbol{r}_i$. $G_{xx}(\boldsymbol{r}_i, \boldsymbol{r}_j')$, $G_{xy}(\boldsymbol{r}_i, \boldsymbol{r}_j')$, $G_{yx}(\boldsymbol{r}_i, \boldsymbol{r}_j')$, and $G_{yy}(\boldsymbol{r}_i, \boldsymbol{r}_j')$ are taken as the independent variables of $\boldsymbol{f}$ in (3), while the expression of $\boldsymbol{f}$ is decided by the dipoles moments $\boldsymbol{M}(\boldsymbol{r}_j')$. For a given set of scanned field $\boldsymbol{H}(\boldsymbol{r}_i)$ ($i = 1,\ldots, M$), now the problem to be solved is changed from finding the equivalent dipole moments to finding the expression of the unknown function $\boldsymbol{f}$.

The advantage of (3) over (2) is that it can be applied for a more general case. For a complex environment, the analytic formula of Green's function is not available or is very time consuming to be calculated. The results in (2) are not accurate for a source in such an environment. However, for most cases, the complex environment Green's function can be numerically calculated by using the free-space Green's functions [$G_{xx}(\boldsymbol{r}_i, \boldsymbol{r}_j')$, $G_{xy}(\boldsymbol{r}_i, \boldsymbol{r}_j')$, $G_{yx}(\boldsymbol{r}_i, \boldsymbol{r}_j')$, and $G_{yy}(\boldsymbol{r}_i, \boldsymbol{r}_j')$]. For example, Green's function of a rectangular cavity can be expressed as the summation of the free-space Green's functions by using the image theory. In this case, the radiated magnetic field still can be written in the form of (3) but with a different unknown function $\boldsymbol{f}$. Due to the powerful self-learning and nonlinear mapping capabilities of the ANN, we can train an ANN to present $\boldsymbol{f}$, so that it can partially consider the imaging effect.

Usually, we only have the magnitude of the radiated magnetic field for most EMI problems. From (3), we can rewrite unknown scalar functions as

$$
|H_x\left(\boldsymbol{r}_i\right)|
$$
$$
= f_x\begin{bmatrix} G_{xx}\left(\boldsymbol{r}_i, \boldsymbol{r}_1'\right), G_{xx}\left(\boldsymbol{r}_i, \boldsymbol{r}_2'\right), \ldots, G_{xx}\left(\boldsymbol{r}_i, \boldsymbol{r}_N'\right), \\ G_{xy}\left(\boldsymbol{r}_i, \boldsymbol{r}_1'\right), G_{xy}\left(\boldsymbol{r}_i, \boldsymbol{r}_2'\right), \ldots, G_{xy}\left(\boldsymbol{r}_i, \boldsymbol{r}_N'\right) \end{bmatrix}
$$
$$(4\text{-}1)$$

$$
|H_y\left(\boldsymbol{r}_i\right)|
$$
$$
= f_y\begin{bmatrix} G_{yx}\left(\boldsymbol{r}_i, \boldsymbol{r}_1'\right), G_{yx}\left(\boldsymbol{r}_i, \boldsymbol{r}_2'\right), \ldots, G_{yx}\left(\boldsymbol{r}_i, \boldsymbol{r}_N'\right), \\ G_{yy}\left(\boldsymbol{r}_i, \boldsymbol{r}_1'\right), G_{yy}\left(\boldsymbol{r}_i, \boldsymbol{r}_2'\right), \ldots, G_{yy}\left(\boldsymbol{r}_i, \boldsymbol{r}_N'\right) \end{bmatrix}.
$$
$$(4\text{-}2)$$
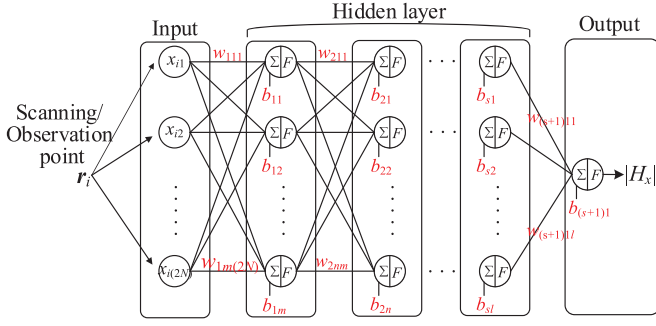
Fig. 2.   Neural network f_x for $|H_x|$ prediction.

In the above-mentioned formula, N is the number of source locations. $|H_x|$ and $|H_y|$ are the magnitudes of the tangential magnetic near-fields on the scanning/observation points. Equation (4) is a nonlinear function. In the following section, we train an ANN to find the expression of f_x and f_y, then we can predict the radiated magnetic field at any observation point.

B. ANN Training

We construct two ANNs (f_x and f_y) to predict $|H_x|$ and $|H_y|$ in (4), respectively. Their structures and training are similar to each other. In the following, we only take f_x as an example. As shown in Fig. 2, the neural network is composed of an input layer, s-hidden layers, and an output layer.

The ANN input is

$$\left[x_{i1}, x_{i2}, \ldots, x_{i2N} \right]$$
$$= \begin{bmatrix} G_{xx}\left(\boldsymbol{r}_i, \boldsymbol{r}_1'\right), G_{xx}\left(\boldsymbol{r}_i, \boldsymbol{r}_2'\right), \ldots, G_{xx}\left(\boldsymbol{r}_i, \boldsymbol{r}_N'\right), \\ G_{xy}\left(\boldsymbol{r}_i, \boldsymbol{r}_1'\right), G_{xy}\left(\boldsymbol{r}_i, \boldsymbol{r}_2'\right), \ldots, G_{xy}\left(\boldsymbol{r}_i, \boldsymbol{r}_N'\right) \end{bmatrix} \quad (5)$$

where $\boldsymbol{r}_1'$–$\boldsymbol{r}_N'$ are predefined. The ANN output is the predicted $|H_x(\boldsymbol{r}_i)|$ at any observation point $\boldsymbol{r}_i$.

In the proposed ANN, we take the set of Green's functions in (5) instead of the direct scanning/observation point $\boldsymbol{r}_i$ as the ANN input. The benefit is that since Green's functions include the electromagnetic radiation formula, they can improve the efficiency of ANN training.

In the ANN of Fig. 2, s denotes the number of hidden layers of the ANN, and $m, n, \ldots, l$ are the numbers of neurons in different hidden layers. $w_{\alpha\beta\gamma}$ is the weight, where subscripts α, β, and γ are the connected hidden layer number, neurons number of the α-layer, and neurons number of the $(\alpha-1)$ layer, respectively. $b_{\alpha\beta}$ is the bias, where subscripts α and β are the hidden layer number and neurons number of the α-layer, respectively.

$\Sigma|F$ is the activation function. Due to the existence of the activation function, the nonlinear mapping ability of the ANNs f_x and f_y is increased. We choose $\tanh(x)$ as the activation function in the following equation. Since the neural network based on Matlab code can only calculate the real number, $\overline{\boldsymbol{G}}(\boldsymbol{r}_i, \boldsymbol{r}_j')$ in (4) is divided into real and imaginary parts

$$\tanh(x) = \frac{e^x - e^{-x}}{e^x + e^{-x}}. \quad (6)$$

The selection of hidden layers and neurons directly determines the quality of the network. If there are too few neurons, f_x and f_y cannot have good learning and information processing capabilities. Too many neurons increase the computation time and increase the risk of overfitting. Therefore, the number of neurons is generally determined by empirical values. So we usually choose three or four hidden layers.

A complex neural network is prone to be overfitting, resulting in poor performance on test sets. Dropout and regularization are commonly used methods to reduce overfitting. For our applications, due to the scanning time limitation, the number of scanned field points is limited. Therefore, different from [13], we use the Bayesian regularization [14] to reduce the overfitting. The regularization preserves all the features of the neural network, reduces the magnitude of the parameters $w_{\alpha\beta\gamma}$, and makes sure that the scanned near-field pattern contributes to the predicted field.

The update of parameters $w_{\alpha\beta\gamma}$ and $b_{\alpha\beta}$ is determined by the backpropagation algorithm of the neural network. During the backpropagation, the cost function is defined as [14]

$$J\left(w_{\alpha\beta\gamma}, b_{\alpha\beta}\right) = \frac{1}{M} \sum_{i=1}^{M} \left[|H_x'\left(\boldsymbol{r}_i, w_{\alpha\beta\gamma}, b_{\alpha\beta}\right)| - |H_x\left(\boldsymbol{r}_i\right)|\right]^2$$
$$+ \lambda\rho\left(w_{\alpha\beta\gamma}\right) \quad (7)$$

where $|H_x'(\boldsymbol{r}_i, w_{\alpha\beta\gamma}, b_{\alpha\beta})|$ is the ANN predicted magnitude of the magnetic field and $|H_x(\boldsymbol{r}_i)|$ is the scanned value. $\rho(w_{\alpha\beta\gamma})$ is the regularization term. $\lambda\,(\lambda > 0)$ is the regularization coefficient, which determines the balance between $|H_x'(\boldsymbol{r}_i, w_{\alpha\beta\gamma}, b_{\alpha\beta})|$ and $|H_x(\boldsymbol{r}_i)|$.

During every training iteration, $w_{\alpha\beta\gamma}$ and $b_{\alpha\beta}$ in (7) are adjusted in order to minimize $J(w_{\alpha\beta\gamma}, b_{\alpha\beta})$. The smaller the $J(w_{\alpha\beta\gamma}, b_{\alpha\beta})$, the more accurate the trained f_x and f_y. We use 70% of the scanned field as a training set and 30% as a test set. During the ANN training, the test set continuously calculates the mean square error with the predicted value of the training set. When the error value is less than 1%, we stop the training. Therefore, M in (7) is the total number of scanning points multiplied by 0.7. The process of forward propagation of the neural network obtains the predicted $|H_x'(\boldsymbol{r}_i, w_{\alpha\beta\gamma}, b_{\alpha\beta})|$, which in turn gets $J(w_{\alpha\beta\gamma}, b_{\alpha\beta})$. After that, the backpropagation process is used, which is based on the gradient descent method. The gradient descent method enables the ANN to find the optimal solution faster while implementing the weight and bias update.

III. NUMERICAL EXAMPLE

In this section, the accuracy of the proposed method is verified by several numerical examples. We use magnetic dipole to represent the EMI radiation source and two metal planes to represent the multireflections environment. In all examples, the ANN training is completed within half an hour.

A. Two Finite Square Metal Planes

The first simulation model is shown in Fig. 3. Two finite square metal planes, each having a side length of 400 mm, are located at $z = 0$ and $z = 100$ mm, respectively. The testing frequency
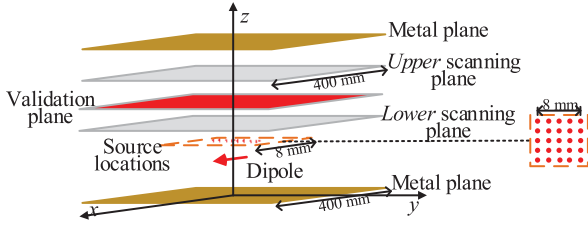
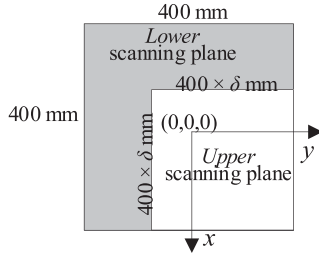Fig. 3.   Magnetic dipole between two finite square metal planes.

Fig. 4.   Top view of two scanning planes.

TABLE I
ERRORS OF PREDICTED FIELD BY USING TWO METHODS WHEN $\delta = 100\%$

ANN				Interpolation			
Height of validation plane	$e_{\|H_x\|}$	$e_{\|H_y\|}$	$e_{\|H\|}$	Height of validation plane	$e_{\|H_x\|}$	$e_{\|H_y\|}$	$e_{\|H\|}$
64 mm	4.96%	2.93%	4.39%	64 mm	8.97%	9.23%	8.46%
65 mm	**0.27%**	**0.37%**	**0.22%**	**65 mm**	**0**	**0**	**0**
73 mm	0.61%	1.32%	0.62%	73 mm	27.16%	34.55%	26.48%
80 mm	**0.42%**	**0.93%**	**0.36%**	**80 mm**	**0**	**0**	**0**
92 mm	4.05%	7.45%	3.77%	92 mm	27.45%	27.97%	26.44%
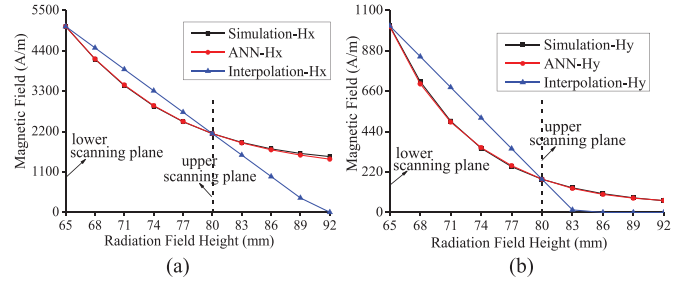
Fig. 5.   (a) H_x and (b) H_y at ($x = -2$ mm, $y = -20$ mm) change with the z-axis for direct simulation, ANN, and interpolation methods.

is 1 GHz. The EMI source is an x-directional dipole located at (0, 0, and 50 mm). The origin is at the center of the lower metal plane.

The source locations $\boldsymbol{r}'_j$ in (2) are defined on an 8 mm × 8 mm plane, which is 1 mm above the dipole and with the z-axis as its center. Five points of $\boldsymbol{r}'_j$ are equally predefined along the x and y directions, respectively, as shown in Fig. 3.

We train the ANN by using the magnetic field magnitude simulated by using the full-wave software on two scanning planes. The heights of the two scanning planes are $z = 65$ mm and $z = 80$ mm, respectively, and with the z-axis as their centers. Near-field magnitude is scanned every 2 mm in the x and y directions. Here, we define the scanning plane with a height of $z = 80$ mm as the upper scanning plane and the scanning plane with a height of $z = 65$ mm as the lower scanning plane.

The lower scanning plane is kept as 400 × 400 mm. In order to verify the robustness of the proposed ANN method, the upper scanning plane is smaller than the lower plane, as shown in Fig. 4. The side length of the upper scanning plane is 400 × δ mm, with $\delta \leq 100\%$. When $\delta = 100\%$, the upper and lower scanning planes have the same size. In some real applications, in order to reduce the scanning time, some parts of the scanning data may be lost. The "δ" is used to demonstrate the advantage of the proposed ANN method over the traditional interpolation method for the lost "δ" part.

We compare the proposed ANN method with the method of cubic spline interpolation. For two methods, the magnetic

field magnitude on two scanning planes is trained or interpolated/extrapolated to predict the magnetic field magnitude on another validation plane, as shown in Fig. 3.

Table I illustrates the errors of predicted fields by using two methods when $\delta = 100\%$, where we take the full-wave simulated magnetic fields on the validation plane as the reference. The rows in red bold represent the predicted field errors on the two scanning planes. It can be seen from Table I that when ANN is used to predict $|H_x|$, $|H_y|$, and $|H|$, the error is much smaller than that of the interpolation method, especially for the fields on validation planes above or below two scanning planes. The error is defined as (8) shown at the bottom of this page, where subscripts cal and ref represent the predicted and reference fields, respectively.

The following Fig. 5(a) and (b) plots the field distribution along the z-axis for three methods. The field decreasing ratio from lower to upper scanning planes is complex since all these fields are in the reactive near-field region of the radiator. It is hard for the interpolation method to predict such a complex field decreasing ratio.

Next, the errors where the ANN and the interpolation methods are used to predict the near-field magnitude when $\delta = 80\%$ are listed in Table II. For this smaller upper scanning plane, the error of the interpolation method increases greatly, while the error of the ANN method is still smaller. Fig. 6 shows the predicted magnitude distribution of the magnetic field at a validation plane

$$e_{|H|} = \sqrt{\frac{\sum_{i=1}^{M}\left(\sqrt{\left|H_x^{\text{cal}}\left(\boldsymbol{r}_i\right)\right|^2 + \left|H_y^{\text{cal}}\left(\boldsymbol{r}_i\right)\right|^2} - \sqrt{\left|H_x^{\text{ref}}\left(\boldsymbol{r}_i\right)\right|^2 + \left|H_y^{\text{ref}}\left(\boldsymbol{r}_i\right)\right|^2}\right)^2}{\sum_{i=1}^{M}\left(\left|H_x^{\text{ref}}\left(\boldsymbol{r}_i\right)\right|^2 + \left|H_y^{\text{ref}}\left(\boldsymbol{r}_i\right)\right|^2\right)}} \tag{8}$$

This article has been accepted for inclusion in a future issue of this journal. Content is final as presented, with the exception of pagination.

WEN *et al.*: NEAR-FIELD PREDICTION IN COMPLEX ENVIRONMENT BASED ON PHASELESS SCANNED FIELDS AND MACHINE LEARNING 5

TABLE II
ERRORS OF PREDICTED FIELD BY USING TWO METHODS WHEN $\delta = 80\%$

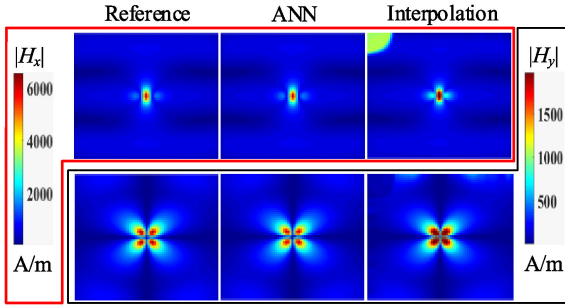| ANN				Interpolation			
Height of validation plane	$e_{|H_x|}$	$e_{|H_y|}$	$e_{|H|}$	Height of validation plane	$e_{|H_x|}$	$e_{|H_y|}$	$e_{|H|}$
64 mm	7.85%	10.47%	7.18%	64 mm	10.61%	9.26%	9.37%
65 mm	**0.97%**	**0.88%**	**0.80%**	**65 mm**	**0**	**0**	**0**
73 mm	1.66%	1.63%	1.42%	73 mm	81.60%	36.58%	74.05%
80 mm	**3.02%**	**2.57%**	**2.60%**	**80 mm**	**159.66%**	**28.59%**	**147.39%**
92 mm	10.12%	10.97%	9.09%	92 mm	296.40%	59.09%	278.24%

Fig. 6. Predicted magnitude distribution of the magnetic field at a height of $z = 73$ mm when $\delta = 80\%$.

of $z = 73$ mm. It can be clearly seen that the interpolation method exhibits a large error in the top-left region of the validation plane, which is just below the "missing region" (nonscanning region) of the upper scanning plane. However, the ANN can accurately predict the field magnitude.

From Tables I and II, and Figs. 5 and 6, we can see that the interpolation method shows a large error when the observation point of the predicted field is far away from the scanning points (above/below the scanning planes, or near the "missing regions" of the scanning planes). On the other hand, since the input of the ANN is Green's function, which contains the source and observation positions, it can predict the complex field decreasing ratio from lower to upper planes, especially when there are constructive and deconstructive interference effects in the reactive near-field region. So the ANN method can predict more accurately than the interpolation method.

The error of the predicted magnetic field magnitude on the validation plane of $z = 73$ mm is compared between the ANN and interpolation methods for different values of δ, as shown in Fig. 7. From these curves, it can be found that the change of ANN error with the size of the upper scanning plane is smoother than that of the interpolation method error. This validates the robustness of the ANN method.

B. Two Infinite Metal Planes

In the second example, two finite metal planes in the first example are replaced by two infinite planes so that there are no edge diffractions, and the frequency is 5 GHz. The distance between the two metal planes is increased to 500 mm. The source dipole is aligned with the center of two metal planes at $z = 50$ mm.
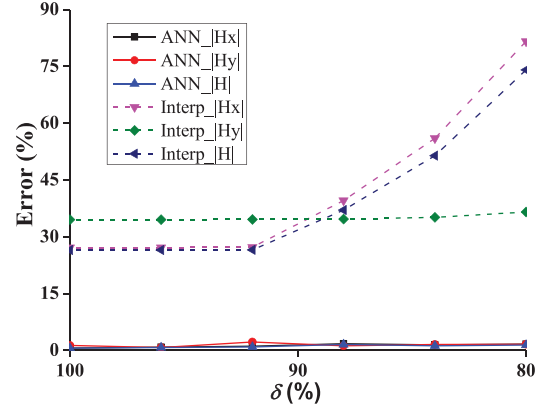

Fig. 7. Errors for the field magnitude on the validation plane of $z = 73$ mm for ANN and interpolation methods.

TABLE III
ERRORS OF PREDICTED FIELD WHEN $\delta = 80\%$

ANN-case 1				ANN-case 2			
Height of validation plane	$e_{|H_x|}$	$e_{|H_y|}$	$e_{|H|}$	Height of validation plane	$e_{|H_x|}$	$e_{|H_y|}$	$e_{|H|}$
145 mm	6.79%	2.89%	6.19%	145 mm	8.56%	1.83%	7.88%
150 mm	**0.26%**	**0.51%**	**0.24%**	**150 mm**	**0.06%**	**0.03%**	**0.06%**
157 mm	5.50%	1.63%	5.11%	157 mm	6.33%	1.10%	5.86%
165 mm	**4.66%**	**2.79%**	**4.19%**	**165 mm**	**7.65%**	**1.63%**	**6.95%**
170 mm	8.64%	3.59%	7.80%	170 mm	11.80%	2.25%	10.80%
ANN-case 3				Interpolation			
Height of validation plane	$e_{|H_x|}$	$e_{|H_y|}$	$e_{|H|}$	Height of validation plane	$e_{|H_x|}$	$e_{|H_y|}$	$e_{|H|}$
145 mm	7.91%	1.93%	7.24%	145 mm	23.77%	20.70%	21.59%
150 mm	**0.09%**	**0.72%**	**0.11%**	**150 mm**	**0**	**0**	**0**
157 mm	8.78%	1.02%	8.30%	157 mm	34.11%	33.58%	33.33%
165 mm	**3.59%**	**0.70%**	**3.21%**	**165 mm**	**75.81%**	**77.54%**	**75.04%**
170 mm	8.22%	1.35%	7.48%	170 mm	101.16%	101.88%	100.28%

Two scanning planes are used. One is at the height of $z = 165$ mm and is called the upper scanning plane, another at the height of $z = 150$ mm is called the lower scanning plane. The size of the lower scanning plane is still 400 mm × 400 mm. The upper left corners of both scanning planes are aligned. Again the ratio between the side lengths of the upper scanning plane and the lower scanning plane is defined as δ.

The source location $\boldsymbol{r}'_j$ is an important parameter for the ANN. It will change Green's functions inputted to the ANN. In this example, the effect of $\boldsymbol{r}'_j$ on the predicted field is analyzed. $\boldsymbol{r}'_j$ is defined on an 8 × 8 mm plane. Three cases are studied: $\boldsymbol{r}'_j$ on $z = 51$ mm with 5 × 5 points (case 1), $\boldsymbol{r}'_j$ on $z = 60$ mm with 5 × 5 points (case 2), and $\boldsymbol{r}'_j$ on $z = 60$ mm with 3 × 3 points (case 3). When $\boldsymbol{r}'_j$ is near the radiation source, the resulting radiation field more closely matches the real radiation field. We generally choose points $\boldsymbol{r}'_j$ not larger than 1/6th wavelength away from the real radiation source.

For $\delta = 80\%$, the prediction errors are illustrated in Table III. When the number and location of $\boldsymbol{r}'_j$ changed, ANN can still create a correct mapping relationship between the observation point and the predicted field, which shows the robustness of the ANN method. However, the interpolation method cannot accurately predict the field outside the scanning regions.
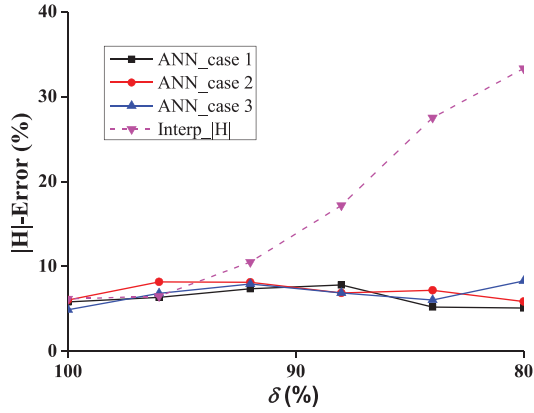
Fig. 8. Errors for the field magnitude on the validation plane of $z = 157$ mm for ANN and interpolation methods.
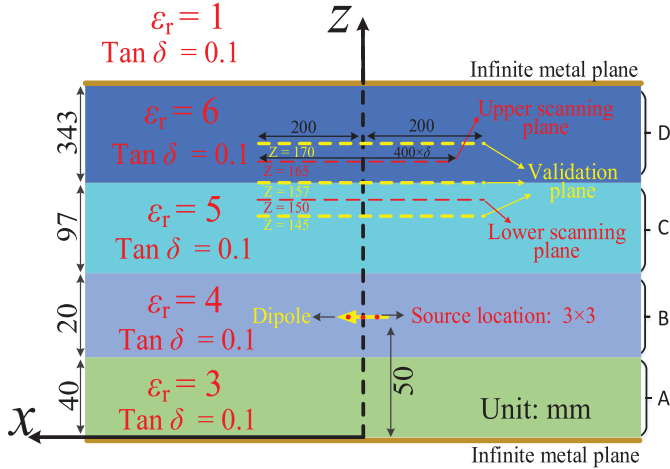

Fig. 9. Magnetic dipole between two infinite metal planes. The area A ($z = 0$ to 40 mm), B ($z = 40$ to 60 mm), C ($z = 60$ to 157 mm), and D ($z = 157$ to 500 mm) are filled with a material with the relative permittivity of 3, 4, 5, and 6, respectively. The dielectric loss tangents of all areas are 0.1.

We plot the error curves for the predicted field magnitude on the validation plane of $z = 157$ mm for ANN and interpolation methods in Fig. 8. Again, the change in the ANN error curve is very flat and is not affected by the incomplete scanning plane. However, the interpolation error is increasing with the reduced δ.

C. Multilayered and Lossy Materials

In this section, the uniform space between two infinite metal planes is replaced by lossy four-layered materials. The dimensions and material parameters of every layer are shown in Fig. 9. The real source is a magnetic dipole in region B. The source locations r'_j is a 3×3 array defined on a 6 mm $\times$ 6 mm plane with the center position (0 mm, 0 mm, 50 mm), which is on the same plane of the real dipole source. The scanning planes are on $z = 150$ and 165 mm, which are in C and D regions in Fig. 9, respectively.

TABLE IV
ERRORS OF PREDICTED FIELD WHEN $\delta = 80\%$, (A) MAGNETIC FIELD AND (B) ELECTRIC FIELD

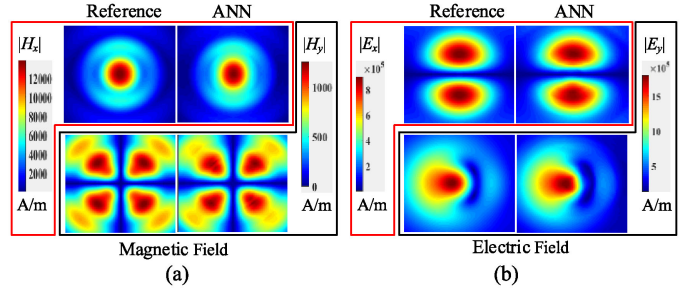| Height of validation plane	$e_{|H_x|}$	$e_{|H_y|}$	$e_{|H|}$	Height of validation plane	$e_{|E_x|}$	$e_{|E_y|}$	$e_{|E|}$
145 mm	10.11%	7.68%	9.74%	145 mm	5.58%	8.56%	6.43%
150 mm	0.17%	0.62%	0.14%	150 mm	0.37%	0.76%	0.53%
157 mm	8.23%	5.96%	7.99%	157 mm	3.30%	3.44%	2.57%
165 mm	2.64%	4.87%	2.47%	165 mm	3.82%	4.50%	4.03%
170 mm	10.85%	9.09%	10.60%	170 mm	6.57%	7.07%	5.86%
(a)				(b)			

Fig. 10. Magnitude distribution of (a) magnetic field and (b) electric field on $z = 157$ mm when $\delta = 80\%$ and dielectric loss tangents is 0.1.

For $\delta = 80\%$, the prediction errors are illustrated in Table IV(a) for different validation planes in regions C and D. In Fig. 10(a), we plot ANN predicted magnetic field pattern on $z = 157$ mm (which is the interface between regions C and D) and compare it with the reference value. Table IV(a) and Fig. 10(a) show that the proposed ANN method is still accurate for the multilayered and lossy materials.

D. Equivalent Electric Dipoles + ANN for Electric Field Prediction

In previous examples, the equivalent magnetic dipoles + ANN are used to predict the magnetic near-field from a real source. In this section, the equivalent electric dipoles + ANN are used to predict the electric near-field from the real source, in order to further verify the generality of the proposed ANN method. The example is the same as that in Section IIIB, except that we filled the material with a loss tangent of 0.1. We also added one more magnetic dipole along the z-direction as the real radiation source.

Green's functions of electric dipoles are used as the input of the ANN. For $\delta = 80\%$, the prediction errors are shown in Table IV(b). In Fig. 10(b), we plot the ANN predicted electric field pattern on $z = 157$ mm and compare it with the reference. They show the ANN method can be used for both electric and magnetic fields' predictions.

IV. MEASUREMENT EXAMPLE

In this section, the ANN method is further validated by the measurement result. Usually, the EMI source is an unintended antenna, so a self-made patch antenna is used as the EMI source. Fig. 11 shows the measured return loss of the patch antenna. Two
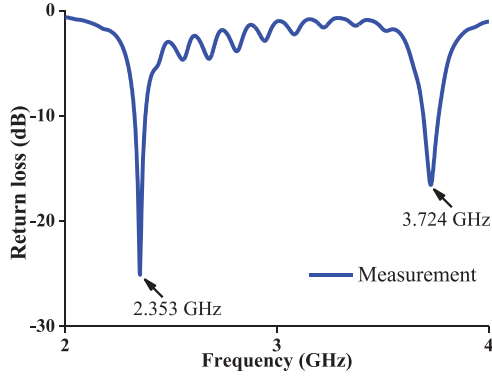
This article has been accepted for inclusion in a future issue of this journal. Content is final as presented, with the exception of pagination.

WEN *et al.*: NEAR-FIELD PREDICTION IN COMPLEX ENVIRONMENT BASED ON PHASELESS SCANNED FIELDS AND MACHINE LEARNING
7

Fig. 11.   Measured return loss of the patch antenna.
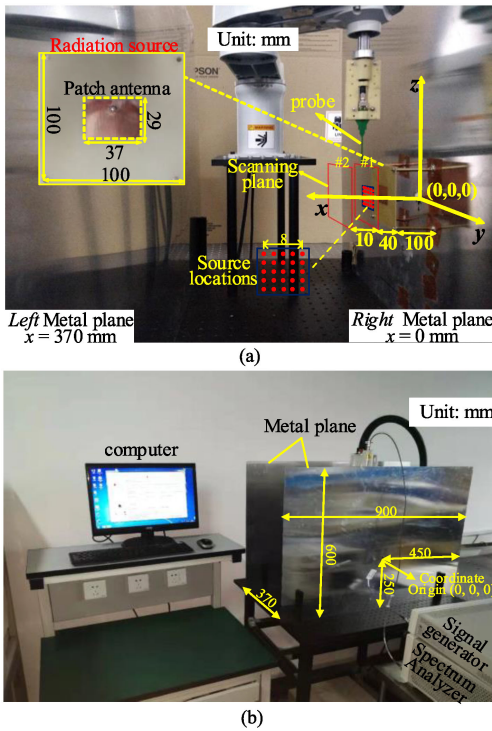
Fig. 12.   (a) Patch antenna and the magnetic probe and (b) near-field scanning system.

TABLE V
ERRORS OF PREDICTED FIELD BY USING THREE METHODS WHEN $\delta = 80\%$

Height of validation plane	ANN			Height of validation plane	Interpolation		
	$e_{|H_x|}$	$e_{|H_y|}$	$e_{|H|}$		$e_{|H_x|}$	$e_{|H_y|}$	$e_{|H|}$
140 mm	0.55%	0.20%	0.21%	140 mm	0	0	0
143 mm	5.37%	2.42%	2.10%	143 mm	13.81%	9.26%	9.46%
145 mm	5.55%	3.57%	2.88%	145 mm	22.45%	15.36%	15.91%
147 mm	4.91%	4.23%	3.20%	147 mm	30.99%	21.03%	22.02%
150 mm	4.85%	5.62%	4.26%	150 mm	42.94%	29.82%	31.20%

Height of validation plane	DE		
	$e_{|H_x|}$	$e_{|H_y|}$	$e_{|H|}$
140 mm	16.6%	7.5%	6.89%
143 mm	12.38%	6.66%	4.15%
145 mm	12.26%	6.91%	4.23%
147 mm	15.32%	7.9%	6.32%
150 mm	24.2%	9.54%	9.86%

Fig. 13.   Magnitude distribution of the magnetic field 145 mm away from the right metal plate when $\delta = 80\%$.
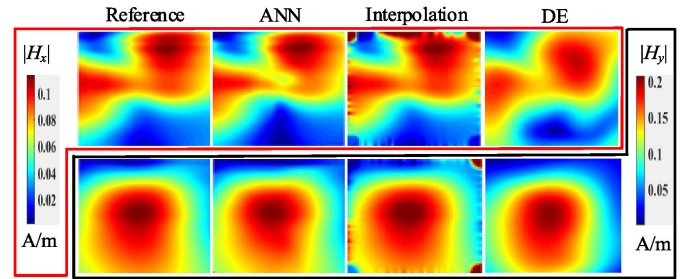
frequencies 2.353 GHz and 3.724 GHz are used as the working frequencies.

As shown in Fig. 12, the patch antenna is placed between two aluminum plates. A near-field scanning system is used to measure the magnetic field of the patch antenna. As shown in Fig. 12(a), the right and left metal planes are at $x = 0$ mm and $x = 370$ mm, respectively. The center of the patch antenna is located at (100 mm, 0 mm, 0 mm). The source locations r'_j are a 5×5 array with the center position (110 mm, 0 mm, 0 mm).

Two scanning planes are used for the ANN training. One is 140 mm away from the right metal plate, which is named the scanning plane #1. Another scanning plane 150 mm away from the right metal plate is named the scanning plane #2. The scanning plane #1 is fixed as 100×100 mm. This time we keep the center of two scanning planes aligned and reduce the size

of the scanning plane #2. The ratio between the side lengths of the two scanning planes is defined as δ. Different from previous numerical examples, here, two magnetic field components are scanned, which are tangential and vertical to the scanning planes, respectively.

In this example, the ANN training is completed within 5 min. Table V presents the errors of the three methods when $\delta = 80\%$. We also apply a global optimization algorithm, the DE method, for comparison. When we reduce the size of the scanning plane #2, the error of the interpolation method is already large than 10%, and the DE method has a larger error than the ANN method. The DE method had been used for source reconstruction in a free-space environment [5].

As can be seen from Fig. 13, the interpolation method has a large error in predicting the fields on the four corners of the validation plane 145 mm away from the right metal plate. The large error regions are related to the "missing regions" of the scanning plane #2. However, the ANN can accurately handle the "missing regions." The DE method gives a blur field pattern than the ANN method does.

Fig. 14 shows the error curves of the magnetic field magnitude on the validation plane 145 mm away from the right metal plate with different δ by using the ANN, DE, and the interpolation methods, respectively. We also verify the calculation error when the operating frequency is 3.724 GHz in Fig. 15. It can be seen that the error of the ANN method is not sensitive to the size of the scanning planes.

This article has been accepted for inclusion in a future issue of this journal. Content is final as presented, with the exception of pagination.

8   IEEE TRANSACTIONS ON ELECTROMAGNETIC COMPATIBILITY
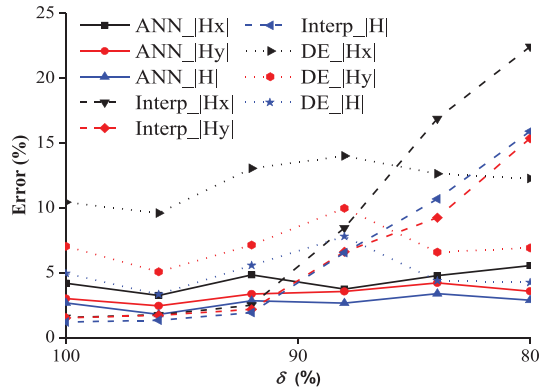

Fig. 14.   Error for the field magnitude on the validation plane 145 mm away from the right metal plate at 2.353 GHz.
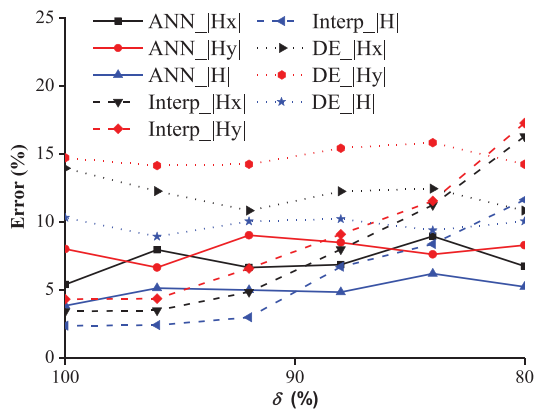

Fig. 15.   Errors for the field magnitude on the validation plane 145 mm away from the right metal plate at 3.724 GHz.

V. CONCLUSION

In this article, we introduce the ANN method to predict near-field radiated from an unknown source in a complex environment with multiple reflections. Most EMI problems include multiple reflections and diffractions of electromagnetic waves in a complex environment, for example, multiple reflections in the shielding box. Such a radiation problem can be explained more clearly from the perspective of Green's function, which is used as the input of the ANN. Using the powerful mapping capabilities of ANN, we build the mapping between the observation point and the magnitude of the magnetic near-field. Compared with the traditional interpolation method and the DE method, the ANN method has better accuracy and robustness.

REFERENCES

[1] X.-C. Wei, *Modeling and Design of Electromagnetic Compatibility for High-Speed Printed Circuit Boards and Packaging*. Boca Raton, FL, USA: CRC Press, 2017.
[2] T. K. Sarkar and A. Taaghol, "Near-field to near/far-field transformation for arbitrary near-field geometry utilizing an equivalent electric current and MoM," *IEEE Trans. Antennas Propag.*, vol. 47, no. 3, pp. 566–573, Mar. 1999.
[3] Y.-F. Shu, X.-C. Wei, R. Yang, and E.-X. Liu, "An iterative approach for EMI source reconstruction based on phaseless and single-plane near-field scanning," *IEEE Trans. Electromagn. Compat.*, vol. 60, no. 4, pp. 937–944, Aug. 2018.
[4] J.-R. Regue, M. Ribo, J.-M. Garrell, and A. Martin, "A genetic algorithm based method for source identification and far-field radiated emissions prediction from near-field measurements for PCB characterization," *IEEE Trans. Electromagn. Compat.*, vol. 43, no. 4, pp. 520–530, Nov. 2001.
[5] W.-J. Zhao *et al.*, "An effective and efficient approach for radiated emission prediction based on amplitude-only near-field measurements," *IEEE Trans. Electromagn. Compat.*, vol. 54, no. 5, pp. 1186–1189, Oct. 2012.
[6] C. Wu, Z. Sun, X. Wang, Y. Wang, B. Kim, and J. Fan, "An Improved dipole extraction method from magnitude-only electromagnetic-field data," *Signal Process.*. [Online]. Available: https://arxiv.org/abs/1901.06776, Accessed on: Jan. 21, 2019.
[7] C. Zhang, J. Jin, W. Na, Q.-J. Zhang, and M. Yu, "Multivalued neural network inverse modeling and applications to microwave filters," *IEEE Trans. Microw. Theory Techn.*, vol. 66, no. 8, pp. 3781–3797, Aug. 2018.
[8] T. Lu, J. Sun, K. Wu, and Z. Yang, "High-speed channel modeling with machine learning methods for signal integrity analysis," *IEEE Trans. Electromagn. Compat.*, vol. 60, no. 6, pp. 1957–1964, Dec. 2018.
[9] H. M. Yao and L. Jiang, "Machine learning based PML for the FDTD method," *IEEE Antennas Wireless Propag. Lett.*, vol. 18, no. 1, pp. 192–196, Jan. 2019.
[10] H. M. Yao, L. J. Jiang, and Y. W. Qin, "Machine learning based method of moments (ML-MoM)," in *Proc. IEEE Int. Symp. Antennas Propag. USNC-URSI Nat. Radio Sci. Meeting*, San Diego, CA, USA, Jul. 2017, pp. 973–974.
[11] Q. Huang and J. Fan, "Machine learning based source reconstruction for RF desense," *IEEE Trans. Electromagn. Compat.*, vol. 60, no. 6, pp. 1640–1647, Dec. 2018.
[12] D. Shi and Y. Gao, "A new method for identifying electromagnetic radiation sources using backpropagation neural network," *IEEE Trans. Electromagn. Compat.*, vol. 55, no. 5, pp. 842–848, Oct. 2013.
[13] Y. F. Shu, X.-C. Wei, J. Fan, R. Yang, and Y.-B. Yang, "An equivalent dipole model hybrid with artificial neural network for electromagnetic interference prediction," *IEEE Trans. Microw. Theory Techn.*, vol. 67, no. 5, pp. 1790–1797, May 2019.
[14] F. Burden and D. Winkler, "Bayesian regularization of neural networks," in *Artificial Neural Networks: Methods and Protocols*, 1st ed., vol. 458, D. J. Livingstone, Totowa NJ, USA: Humana Press, 2008. pp. 23–42.

Jun Wen (Student Member, IEEE) received the B.S. degree in automation from Inner Mongolia University, Hohhot, China, in 2018. He is currently working toward the M.S. degree in control engineering with Inner Mongolia University, Hohhot, China.

His current research interests include electromagnetic modeling and simulation based on artificial neural network and near-field electromagnetic interference.

Xing-Chang Wei (Senior Member, IEEE) received the Ph.D. degree in electrical engineering from Xidian University, Xi'an, China, in 2001.

From 2001 to 2010, he was with the A∗STAR Institute of High-Performance Computing, Singapore, as a Research Fellow, Senior Research Engineer, and Research Scientist. In 2010, he joined Zhejiang University, Hangzhou, China, as a Full Professor. He has authored or coauthored one book, one book chapter, and more than 130 papers published in IEEE transactions and international conferences. His main research interests include electromagnetic compatibility modeling and testing, power integrity, and signal integrity simulation and design.

Dr. Wei is the recipient of the Singapore Institution of Engineers Prestigious Engineering Achievement Award, in 2007 for his contribution to the development of the reverberation chamber for EMC measurement, New Century Professional Award from China Ministry of Education, and numerous awards from the IEEE international conferences, including APEMC, EMC Compo, SPI, EuCAP, IWS, and ICEPT. He was TPC Co-Chair of 2010 IEEE EDAPS, Technical Paper Co-Chair of 2018 IEEE APEMC Symposium, Program Chair and Finance Chair of 2012 and 2016 APEMC, respectively, and TPC members of EMC related international conferences.

Yong-Liang Zhang received the B.S. and Ph. D. degrees in electrical engineering from Xidian University, Xi'an, China, in 2009 and 2014, respectively.

He is currently with the College of Transportation, Inner Mongolia University, Hohhot, China. His research interests include passive microwave/millimeter-wave device, filtering antenna, smart antennas, reconfigurable antennas, and frequency selective surfaces, electromagnetic compatibility, and metasurface-based antenna.

Tian-Hao Song received the B.S. degree in information engineering from Soochow University, Suzhou, China, in 2018. He is currently working toward the Ph.D. degree in electrical engineering with Zhejiang University, Hangzhou, China.

His current research interests include signal integrity, near-field electromagnetic interference, and electromagnetic compatibility for high-speed circuits.